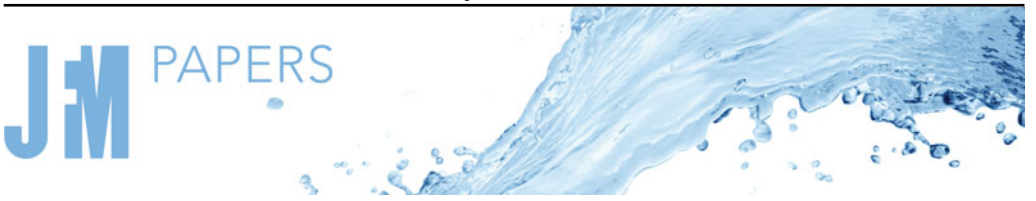
J. Fluid Mech. (2026), *vol.* 1041, A32, doi:10.1017/jfm.2026.11951



Boundary-layer flow dynamics of propulsive flapping foils with increasing Reynolds numbers

Andhini Novrita Zurman-Nasution[1], **Gabriel D. Weymouth**[2] and **Bharathram Ganapathisubramani**[1]

[1]School of Engineering, University of Southampton, Southampton SO16 7QF, UK

[2]Ship Hydromechanics, TU Delft, Delft, The Netherlands

Corresponding author: Andhini Novrita Zurman-Nasution, a.zurman-nasution@soton.ac.uk

(Received 13 August 2025 UTC; revised 6 May 2026 UTC; accepted 11 July 2026 UTC)

We study flapping foils at optimally propulsive Strouhal number $St = 0.3$ with increasing chord-based Reynolds number $Re = 10^4$, 10^5 and 10^6 to examine changes in their unsteady boundary layers. Despite being prescribed the same freestream, the inner boundary-layer characteristics exhibit different trends due to the generation of leading-edge vortices (LEVs) and their advection into the downstream flow. Propulsive flapping foils show an extended laminar region known as the relaminarisation, during which the velocity profiles deviate from the standard log law. This relaminarisation is accompanied by a significant decrease in the cyclic fluctuation of the wall friction coefficient and an increase in the shape factor, while the freestream velocity increases under favourable pressure gradient conditions. This phenomenon intensifies with increasing *Re*. We found that higher *Re* produces smaller LEVs in greater quantities, with a more rapid but stable breakdown, without resulting in a more chaotic turbulent downstream. This study strongly indicates that the relaminarization could extend beyond $Re = 10^6$ as predicted by Fukagata *et al.* (2023 *Annu. Rev. Fluid Mech.*, vol. 56, pp. 69–90). The results support the potential for further exploration of flapping foils at high *Re* for noise and drag reduction.

Key words: propulsion, boundary layers, vortex dynamics

1. Introduction

Interest in flapping foil studies has been increasing for more than two decades in the fields of optimal propulsion for aerial and underwater robots, swimming/flying gaits, and

© The Author(s), 2026. Published by Cambridge University Press. This is an Open Access article, distributed under the terms of the Creative Commons Attribution licence (https://creativecommons.org/licenses/by/4.0/), which permits unrestricted re-use, distribution and reproduction, provided the original article is properly cited.

https://doi.org/10.1017/jfm.2026.11951 Published online by Cambridge University Press

recently for drag/noise reduction and flow control. To apply this research at an industrial scale will require a massive increase in the size of the foil and the Reynolds number of the flow. However, propulsive flapping foil flow of combined pitch–heave motions at $Re \gtrsim 5 \times 10^5$ has not been extensively studied, either numerically or experimentally, motivating an in-depth investigation.

Flapping foils are reported to be optimally propulsive in the range $0.2 < St < 0.4$ (Triantafyllou *et al.* 1993; Eloy 2012) for swimming animals with oscillating lift-based propulsion. These St ranges generate the highest efficiency and exhibit two-dimensional (2-D) flow with relatively small leading-edge vortices (LEVs) for pitching–heaving kinematics (Zurman-Nasution *et al.* 2020). The flow surrounding a flapping foil is affected by its motion, and studying its effect on the boundary-layer region is expected to reveal the details comprehensively.

Many studies have been published for the characteristics of the boundary-layer flow that we can relate to flapping foil flow, such as the flow over a flat plate and channel flow (Clauser 1954), curved flow and stationary foils (Coles 1956; Mukund *et al.* 2006; Devenport & Lowe 2022), unsteady flow and boundary-layer separation (Na & Moin 1998; Ambrogi *et al.* 2022). These studies describe the changes in the flow due to pressure gradients, mostly at the constant zero, adverse and favourable pressure gradients, abbreviated as ZPG, APG and FPG respectively. As the name suggests, the ZPG indicates no pressure change, or $\mathrm{d}Cp/\mathrm{d}x = 0$, where Cp is the pressure coefficient. Meanwhile, the APG indicates the increase of pressure nominal to the flow direction ($\mathrm{d}Cp/\mathrm{d}x > 0$), and the opposite for FPG ($\mathrm{d}Cp/\mathrm{d}x < 0$). The APG also indicates the local flow deceleration, while FPG is related to the acceleration.

As the flow over a foil surface is curved, we are interested in several studies about turbulent flow under the strong influence of pressure gradients. Several studies by Patel & Head (1968), Warnack & Fernholz (1998) and Mukund *et al.* (2006) emphasised the phenomenon of relaminarisation under the influence of a strong FPG. The phenomenon is seen as a transitional condition, with the suppression of near-wall turbulence and the emergence of laminar-like velocity profiles. Narasimha & Sreenivasan (1979) called it the reversion, as the result of pressure force domination over slowly responding Reynolds stresses in the outer region, accompanied by laminar generation inside the boundary layer, and stabilised by the flow acceleration. The characteristics of flow undergoing FPG are thus related to the stabilisation through acceleration inside the boundary layer, or vice versa, APG is related to destabilised flow. The variable to indicate this relaminarisation phenomenon is $\Delta_P = -\mathrm{d}p/\mathrm{d}x^+ = -(\nu/\rho u_\tau^3)(\mathrm{d}p/\mathrm{d}x)$, which has characteristics of inner layer u_τ values at $\Delta_P > 0.018$ (Patel & Head 1968; Uzun & Malik 2021). Mukund *et al.* (2006) use an acceleration parameter $K = (\nu/\rho u_e^2)(u_e/\mathrm{d}x)$ that is not universal, as it involves the parameter of boundary-layer edge velocity u_e affected by the freestream.

An essential feature of flapping foil flow is the generation of LEVs that resemble the separation bubbles. Several experimental studies of turbulent separation bubbles provide insight into how the changes in pressure gradient affect the turbulent flow, such as the blow-and-suction experiments in channel flow (Na & Moin 1998). Recently, Ambrogi *et al.* (2022) concluded that the flow reversal leads to a hysteresis effect at a certain reduced frequency. There is also a review study reported on multiple blow-and-suction experiments by Fukagata *et al.* (2023) for drag reduction. At a generally low Reynolds number flow, the LEV generated by a propulsive flapping foil is similar to a laminar separation bubble or a 2-D LEV, exhibiting a smooth structure across the span. However, at a higher Reynolds number case or for large-scale flapping foil, the LEV is expected to develop into a turbulent separation bubble with three-dimensional (3-D) flow characteristics, such as irregular spanwise structures, or ultimately, chaotic and unstable vortex structures.

https://doi.org/10.1017/jfm.2026.11951 Published online by Cambridge University Press

Whether 2-D or 3-D LEVs on the foil are driven by the flapping kinematics, and also presumably by the Reynolds numbers, their influences on the boundary layer remain poorly understood.

Only a limited number of experimental and numerical studies have focused on the boundary layer of a flapping foil or a swimming animal, mostly because of the set-up cost and extensive requirements to zoom in on the region near the wall boundary. The higher the Reynolds number, the more challenging and complex this study can become. Large mammals, such as dolphins and whales, swim at a range of body length $Re \approx 10^6$ and beyond, indicating that turbulent flow most probably occurs on their flapping flukes. Research on smaller Reynolds number ranges has been conducted through experiments such as the fish-robot experiment by Triantafyllou *et al.* (2002), and even using live fishes (Taneda & Tomonari 1974; Anderson *et al.* 2001; Yanase & Saarenrinne 2015). Studies of foils with imposed kinematics at $Re \gtrsim 5 \times 10^5$ are available (Münch *et al.* 2010; Benton & Visbal 2018), but they do not focus on propulsive flapping or on boundary-layer dynamics. We address this gap by extensively studying the boundary layer of a propulsive flapping foil, focusing on the changes in inner boundary-layer parameters affected by the outer-layer forcing or the freestream, and how they correlate with increasing Re.

The remainder of the paper is organised as follows. We give the methodology in § 2, describing the numerical methods, resolution, validation procedures and definitions. Section 3 presents experimental comparisons, and examines LEV coherence, boundary-layer velocity profiles, relaminarisation behaviour and applicable diagnostic criteria. Section 4 concludes with the main findings and their implications.

2. Methodology

2.1. *Simulation arrangement for flapping foils*

An NACA0016 with chord length C and foil thickness $0.16C$ oscillates sinusoidally with combined pitch and heave motions. The pitch pivot point is at $0.25C$ from the foil leading edge. The foil is placed in a uniform flow with inflow speed U_∞ and fluid density ρ. The chord-length-based Reynolds number ($Re = U_\infty C/\nu$) is progressively increased from 10^4 to 10^5 to 10^6, with ν as kinematic viscosity. Other references besides the chord length will be indicated by a subscript on Re. We study the optimal propulsive Strouhal number $St = 2Af/U_\infty = 0.3$, where $2A$ is the peak-to-peak amplitude at the trailing edge, and f is the flapping frequency. This St lies within the range of minimal spanwise perturbations that lead to predominantly 2-D flow at low Re (Zurman-Nasution *et al.* 2020).

The foil oscillates with sinusoidal kinematics constructed from heaving $H(t)$ and pitching $\theta(t)$ motions as

$$H(t) = A\sin(2\pi f t), \tag{2.1}$$

$$\theta(t) = \theta_0 \sin(2\pi f t + \pi/2), \tag{2.2}$$

$$\theta_0 = \sin^{-1}\left(A/(0.75C)\right), \tag{2.3}$$

where $A = 0.25C$. We fixed the flapping reduced frequency as $k = fC/U_\infty = 0.6$. This relatively high reduced frequency allowed us to minimise the peak-to-peak amplitude for the trade-off of our computing capability at $Re = 10^6$ while keeping maximum efficiency η and thrust coefficient C_T at the chosen St. The hydrodynamics performances are tabulated in table 1. The effective angle of attack $\alpha(t) = -(\tan^{-1}(\mathrm{d}H(t)/\mathrm{d}t) - \theta(t))$

https://doi.org/10.1017/jfm.2026.11951 Published online by Cambridge University Press

Re	Mean thrust coefficients ($\overline{C_T}$)	Mean power coefficients ($\overline{C_{Pow}}$)	Efficiency η
10^6	0.61	1.52	0.40
10^5	0.65	1.66	0.39
10^4	0.60	1.60	0.38

Table 1. Hydrodynamic performance statistics at $St = 0.3$. Here, $C_T = -F_X/(0.5\rho S_p U_\infty^2)$, $C_{Pow} = P/(0.5\rho S_p U_\infty^3)$ and $\eta = \overline{C_T}/\overline{C_{Pow}}$, where F_X is the integrated streamwise force, S_p is the foil's planform area, P is integrated power and ρ is density. The overline indicates the total cycle average, and C_T includes both pressure and viscous forces.

defines the evolution of the foil's angle of attack along the cycle (Hover *et al.* 2004), where $\alpha_{eff} = \max(|\alpha(t)|) = 23.83°$.

2.2. *Solver and simulation convergence*

This study uses the boundary data immersion method (BDIM) solver package (Maertens & Weymouth 2015) with second-order accuracy in space near the solid–fluid boundary, an improvement of Weymouth & Yue (2011). The BDIM uses implicit large-eddy simulations, Cartesian grids, finite volume, and the Quick scheme that has been proven to accurately predict the integrated forces on moving bodies in Maertens & Weymouth (2015) up to $Re = 10^5$. The immersed boundary thickness area in BDIM is $\epsilon/\Delta Y = 2$, where ΔY is the smallest cell unit, and ϵ is the BDIM kernel radius. Here, ϵ is a transition region between the solid and fluid, where the velocity field is smoothly blended with the prescribed kinematics while the Navier–Stokes equations are solved in a regularised form. Readers are referred to Maertens & Weymouth (2015) for further details of BDIM formulation.

The foil is placed within a uniform Cartesian grid region with $\Delta X/\Delta Y = \Delta Z/\Delta Y = 2$, where X, Y, Z are the global coordinates in the streamwise, lateral and spanwise domains of the inflow. Outside the uniform-grid domain, the grids stretch with maximum ratio 8 % in $-3C \leqslant X \leqslant 11C$ and $-3C \leqslant Y \leqslant 3C$. We make sure that the uniform-grid domain in Y encloses the foil at the maximum trailing-edge amplitude, the boundary-layer zone and the near wakes. The X uniform-grid domain covers at least one von Kármán vortex pair, but five pairs in the whole domain. The size of the uniform grids is set such that the first grid points outside the foil are always inside the linear boundary-layer region, with $y^+ \leqslant 7.1$ for the worst case at $Re = 10^6$, where $y^+ = yu_\tau/\nu$ is the viscous distance, and u_τ is the friction velocity. The first grid points reach the resolutions defined in more detail in table 2 after flapping cycles where the simulations converge. A grid convergence study is further discussed in Appendix B.

The x, y, z coordinates are local tangential, normal and spanwise distances, respectively, to the solid boundary, as depicted in figure 1(*a*). The spanwise grid domain is uniform with periodic boundary conditions, and the domain span or span length S is set to be minimal for computing cost, but the resolution is kept such that $S \geqslant 100\nu/u_\tau$ to sufficiently capture the smallest structure in the spanwise direction based on Jiménez & Moin (2006). This specifically constrains the span length at the highest Re, while other Re cases have sufficiently larger spans with resolution $S/\Delta Z$. Although the minimal spanwise extent relative to outer-layer scales at $Re = 10^6$ may restrict the development of larger 3-D structures and secondary instabilities, the near-wall dynamics remains resolved, including LEV formation and breakdown to capture the vortex–boundary-layer interaction. The consistent hydrodynamic performance across Reynolds numbers (table 1)

https://doi.org/10.1017/jfm.2026.11951 Published online by Cambridge University Press

Re	Resolution $C/\Delta Y$	y^+ range	y^+ mean	Span length/C	3-D simulation cycles	Phase-averaged cycles	Simulation costs (cores)
10^4	700	[0.02, 2.7]	1.2	0.5	70	70	416 : 7.2
10^5	5000	[0.02, 2.2]	1	0.1	67	67	720 : 17.8
10^6	8555	[0.1, 7.1]	3.5	0.009	16	6	1200 : 63

Table 2. Resolution for three Re values. The y^+ values are the first grid inside BDIM ϵ. The total cycles of 3-D simulations exclude the preceding 2-D simulations. The phase-averaging for $Re = 10^6$ is conducted at the last 6 cycles to exclude the transient phases. The last column contains information of CPU-core usage and simulation length in hours per cycle.

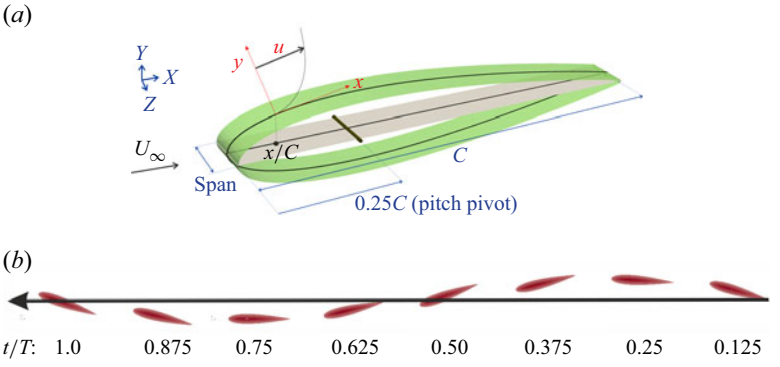


Figure 1. (*a*) Diagram of the foil and the streamwise velocity U with its normal (y) and tangential (x) axes. (*b*) Flapping foil phases in time t over a cycle period T. For discussion, phases t correspond to the upper side of the foil, while the lower part experiences $t \pm 0.5T$.

and preserved flapping-frequency response (see Appendix C) indicate that the primary propulsive mechanisms are unaffected. Each 3-D simulation, continued and expanded from a 15-cycle 2-D simulation, converges in approximately 6–10 cycles. A spanwise perturbation with magnitude $0.02U_\infty$, composed of zero-mean random fluctuations, is added at the start of the 3-D simulations to trigger secondary instabilities.

We discuss the comparison for $Re = 10^4$, 10^5 and 10^6 for this study in § 3. We limit Re to one million due to the high computational cost of wall-resolved large-eddy simulations, and table 2 shows that our near-wall resolutions and number of cycles had to be reduced for that case compared to the lower Re. Later in § 3, we notice that the phase averaging at $Re = 10^6$ for six cycles was insufficient to completely smooth out the fluctuations, and might need more resolution near the trailing-edge region. However, this limitation does not change the conclusion of the study, especially the trends with increasing Re. Similarly, the lack of resolution affects only the flow downstream near the outlet boundary.

2.3. *Cycle phases*

In the results discussion, we will present data for 32 phases per cycle as per figure 1(*b*). The results will only represent the upper side of the foil experiencing phases per cycle t/T. Later, we show the span and phase averaging results as presented in table 2 for phase-averaged cycles. Since the foil is symmetrical, the lower side experiences the same states as the upper side after a half-cycle or $t/T + 0.5$. In the results, the first phase starts when the foil moves upwards, $t/T = 0.03125$, and ends at phase $t/T = 1$ when the foil's

https://doi.org/10.1017/jfm.2026.11951 Published online by Cambridge University Press

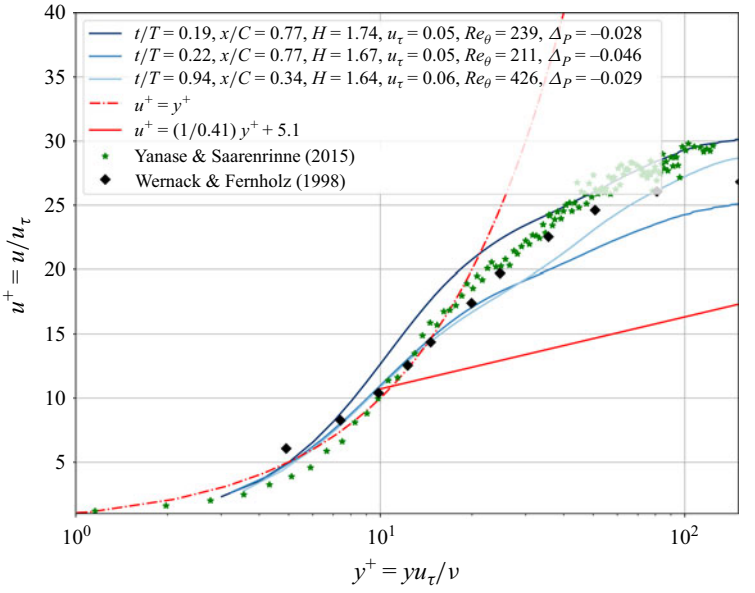


Figure 2. Velocity profile comparison of the current study (blue lines) with experiments. The current study is at $Re = 10^5$ at several t/T phases and x/C locations. Presented experiments are from the rainbow trout experiment by Yanase & Saarenrinne (2015) on convex motion (unknown u_τ and Re_θ), and the turbulent boundary layer at FPG by Warnack & Fernholz (1998). Despite having different u_τ, the profiles show similar extended laminar regions.

pivot is at location $Y = 0$. The cycle restarts after $t/T = 1$ or is equivalent to $t/T = 0$. The projected positions are presented in 100 x/C equispaced locations on the foil as depicted in figure 1(*a*).

Later in the results section, we present parameters needed to compute the boundary-layer edge velocity u_e. We use the method of velocity reconstruction from pressure data based on Bernoulli's equation by Griffin *et al.* (2021) to locate the boundary-layer edges (δ_e), while the velocity field is not modified. It has been compared with other methods, such as by Uzun & Malik (2021). This method is suitable because the velocity profiles expand and retract dynamically along the phases and locations, as explained in Zurman-Nasution *et al.* (2024).

3. Results

3.1. *Comparison with experiments*

Despite the scarcity, we found comparison studies for our flapping foil studies at $Re \geqslant 10^5$, such as the experiment of swimming rainbow trout by Yanase & Saarenrinne (2015) at body length $Re_{BL} \approx 10^5$, and the study of FPG effects on axisymmetric turbulent boundary layers by Warnack & Fernholz (1998). The rainbow trout experiments recorded unsteady velocity profiles, while the FPG is a quasi-steady experiment. Despite the steadily imposed pressure gradient, the FPG experiment provides a gradual boundary-layer transition towards relaminarisation, comparable to the unsteady cases of a flapping foil and a swimming fish. By matching the boundary-layer characteristics, such as the shape factors $H = \delta^*/\theta$ (ratio of displacement $\delta^* = \int^{\delta_e} (1 - (u/u_e))\, \mathrm{d}y$ to momentum thicknesses $\theta = \int^{\delta_e} (u/u_e)(1 - (u/u_e))\, \mathrm{d}y$), we recover similar velocity profiles as shown

https://doi.org/10.1017/jfm.2026.11951 Published online by Cambridge University Press

in figure 2. One sample in the current study is relatively close to the momentum thickness Reynolds numbers Re_θ (Warnack & Fernholz 1998), but the friction velocities u_τ are completely different. There is no information on Re_θ and u_τ from the experiments of swimming rainbow trout for comparison.

We found that the velocity profiles in our flapping foil study exhibit similarities to the rainbow trout experiment, including a distinct extended laminar region beyond $y^+ = 11$. Most velocity profiles in the present study show extended laminar regions. While deviations from ZPG log law are expected in non-equilibrium boundary layers, the present study examines systematically the characterisation of laminar-like velocity profiles across a wide range of Reynolds numbers. Figure 2 shows the shape factor $H \approx 1.7$, considered far lower than the classical laminar profile ($H \geqslant 2.6$). In fact, this phenomenon is considered in a transitional state between turbulent and laminar under the influence of accelerating flow mentioned by Schlichting & Kestin (1979). It explains why the flapping foil's velocity profiles are similar to Warnack & Fernholz (1998) and Balin & Jansen (2021) in their quasi-steady experiment for examining the relaminarisation cases, showing laminar-like profiles. In the case of a stationary foil at $Re = 10^5$ and angle of attack lower than $\alpha_{eff} = 23.8°$, the flow would have experienced strong separation or stall-triggered turbulent flow as seen in the study of Vinuesa *et al.* (2018). Flapping foils are known to experience dynamic stall, which delays the separation.

Patel & Head (1968) referred to the relaminarisation phenomenon as a reverse transition, and suggested that its onset happens in the boundary layer mostly under a strong FPG, and is independent of the boundary-layer characteristics such as H or Re_θ. Apart from similar H, both u_τ and Re_θ in this study can be different, as shown in figure 2. However, the values of non-dimensionalised pressure gradient Δ_P are below the threshold -0.018, indicating the influence of APG. Patel & Head (1968) (on p. 376) show a similar example where strong pressure gradients cause a major departure from the semi-logarithmic law, not only for APGs but also for FPGs.

These comparisons provide a validation of a similar phenomenon seen in flapping foil profiles with the unsteady and quasi-steady experiments, i.e. the strong influence of pressure gradients, and the appearance of an extended laminar region. In § 3.4, we will examine the effects of pressure gradient on flapping foils, and discuss the mechanism that explains the extension of the viscous region beyond $y^+ = 11$, as well as its relationship to relaminarisation. The next subsection discusses the effect of the pressure gradient originating from the outer part of the boundary layer.

3.2. *Freestream region influence*

Figure 3 shows the pressure and velocity variation at height $y = 0.1C$ above the foil, or the freestream region, as a function of length along the foil, and phase in the motion cycle across the three Reynolds numbers.

The pressure coefficient heat map in figure 3(*a*) shows that the suction region (negative Cp values) occurs in phases $0.3 \leqslant t/T \leqslant 0.7$ and is fairly uniform from the leading to the trailing edges. Each side of the foil experiences alternately the pressure side or the suction side once each per cycle.

In figure 3(*b*), the local velocities u/U_∞ at height $0.1C$ show that each foil side experiences alternating high (a peak) or low (a valley), but they are not uniform along the chord length. Each foil side can experience different velocities in one phase. For example, at phase $t/T \approx 0.5$, the leading edge experiences a much higher velocity than the inflow with $u > 1.75U_\infty$, while the trailing edge experiences $u < 0.5U_\infty$. The velocity contours show an inclination of approximately a half-cycle ($0.5T$) from the leading edge at

https://doi.org/10.1017/jfm.2026.11951 Published online by Cambridge University Press

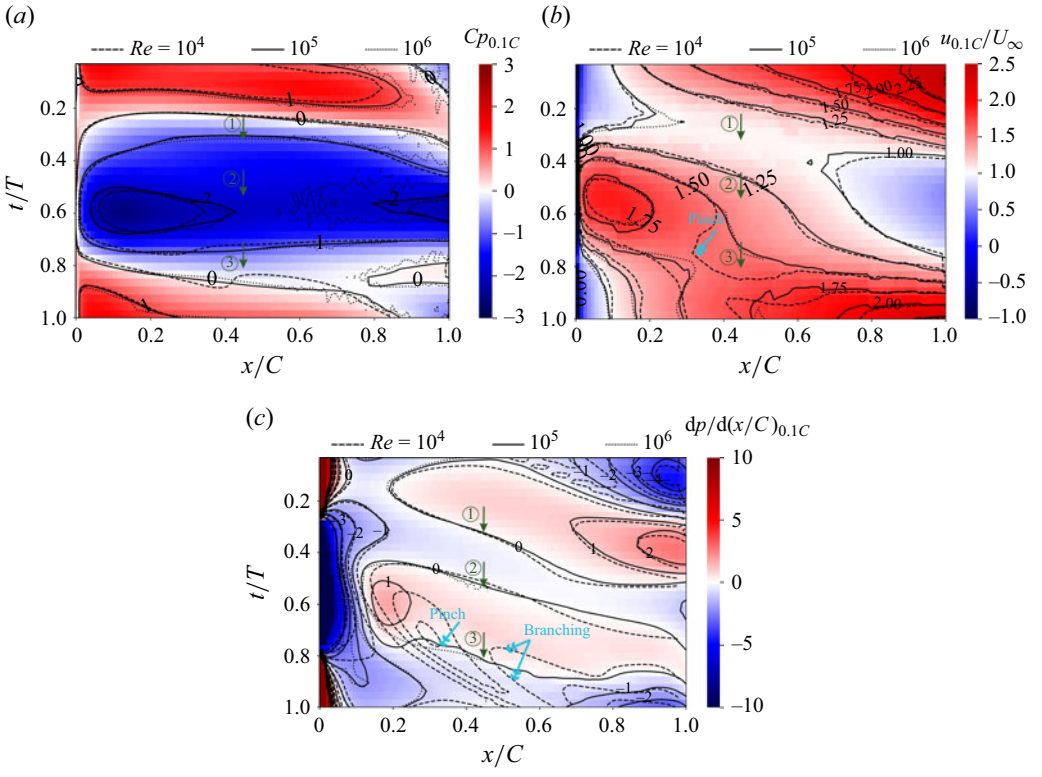


Figure 3. The heat maps of (*a*) pressure coefficients Cp, (*b*) streamwise local velocities u/U_∞, and (*c*) pressure gradient $\mathrm{d}p/\mathrm{d}(x/C)$ at height $0.1C$ from the upper side wall of the foil at $Re = 10^5$. The horizontal axis is the projected position on the upper foil x/C representing space, and phase t/T on the vertical axis represents the time evolution of the flow. All are span- and phase-averaged data, with selected contour lines to compare different Re. At height $0.1C$, the heat map represents the freestream region. Double-headed arrows (cyan) show the deviated contour at $Re = 10^4$ due to an LEV. Green arrows with numbers are given for later discussion in figure 5.

$t/T \approx 0.5$ to the trailing edge $t/T \approx 1$. This half-cycle inclination is due to the sinusoidal flow advection from the prescribed flapping kinematics.

We also present the pressure gradient evolution $\mathrm{d}p/\mathrm{d}(x/C)$ in figure 3(*c*) at height $0.1C$. Each position of x/C alternates twice per cycle between APGs in red and FPGs in blue, with two distinct APG regions. Strong but narrow APG and FPG regions happen near the leading edge, while the trailing edge is clipped by the wake. The trend of APG and FPG is inclined similarly to the velocity, following the flow advection trend.

At height $0.1C$, increasing Reynolds numbers do not show a significant difference, as shown by the majority of the contour lines of different Re. There is data noise for $Re = 10^6$, especially near the trailing edge, due to the limited number of cycles for phase averaging. We can see that the variation is minimal for all Re, with an exceptional deviation caused by a single LEV affecting the $y = 0.1C$ region for $Re = 10^4$. The arrow marked 'Pinch' in figures 3(*b*) and 3(*c*) at $t/T = 0.75$ and $x/C = 0.34$ shows the contour deviation of $Re = 10^4$ from other Re cases, causing a 'pinched' contour of $u/U_\infty = 1.5$. At the subsequent phase and at $x/C = 0.45$, the APG region for $Re = 10^4$ starts 'branching' (see figure 3*c*). The upper branch with $\mathrm{d}p/\mathrm{d}(x/C) > 0$ follows advection similar to that of the other higher-Re cases, while the lower branch shows an elongated APG region extending

https://doi.org/10.1017/jfm.2026.11951 Published online by Cambridge University Press

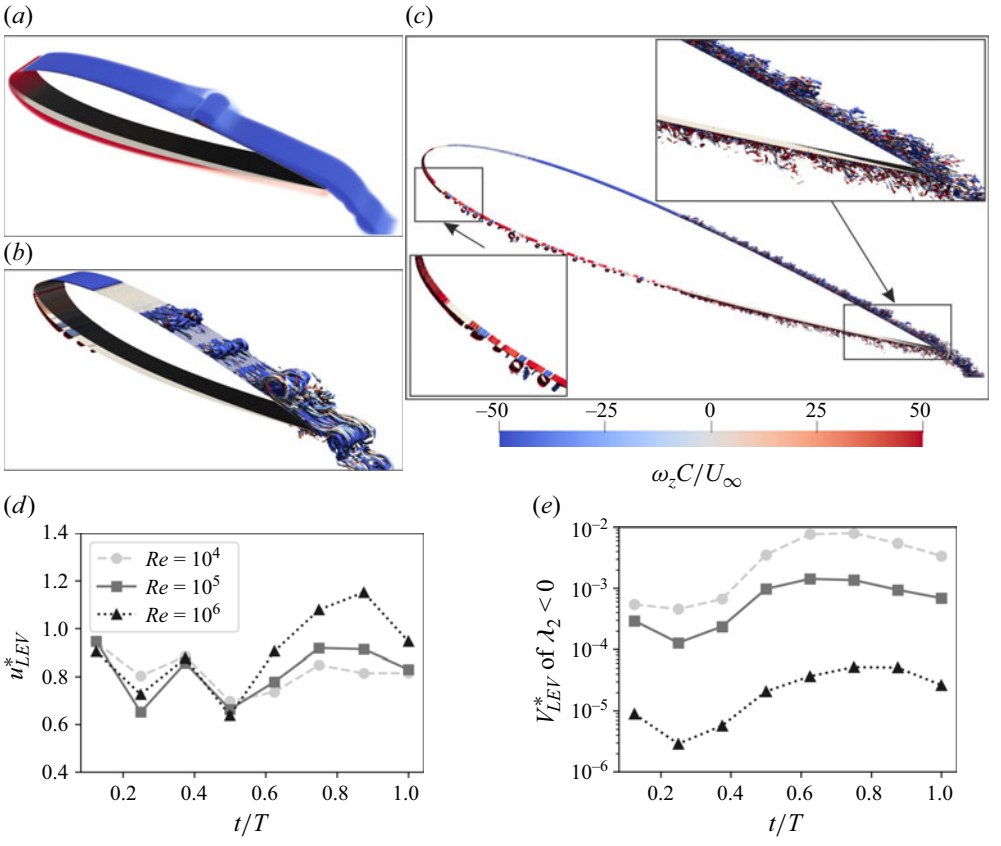


Figure 4. Instantaneous vortex structures are represented by (*a*) volume render of spanwise vorticity of $Re = 10^4$, (*b*) contour of 0.1 % maximum λ_2 of $Re = 10^5$, and (*c*) $Re = 10^6$. The upper foil experiences phase $t/T = 1$ or the last cycle, while the lower foil experiences $t/T = 0.5$. Colours represent spanwise vorticity normalised by the chord and the freestream velocity. The LEV advection is quantified by (*d*) the ω_z-weighted streamwise velocity $u^*_{LEV} = (\int (u_x/U_\infty)\,|\omega_z|\,\mathrm{d}V_{LEV})/(\int |\omega_z|\,\mathrm{d}V_{LEV})$, and (*e*) the normalised LEV volume $V^*_{LEV} = (1/C^3)\int \mathrm{d}V_{LEV}$, where u_x is the local streamwise velocity parallel to C. The integration domain of V_{LEV} is restricted to the upper side of the foil, $0 < x/C < 1$, $y < 0.1C$, and $\lambda_2 < 0$ for LEV centroid locations.

downwards. This branch undergoes a shorter distance $\Delta x/C$ over the same interval $\Delta t/T$ as the upper branch, indicating a slower advection caused by an LEV. A large LEV is advected more slowly than the half-cycle advection due to its size. We discuss further in the next subsection how larger vortices tend to be advected more slowly than smaller ones.

3.3. *Vortex structures*

Increasing Reynolds numbers produce very distinct vortex structures generated by flapping foils, especially the LEVs. Figure 4 presents the instantaneous vortex structures at $t = T$. The vorticity at $Re = 10^4$ is essentially 2-D (see figure 4*a*), matching the results from previous low-*Re* studies in the optimal $0.15 \leqslant St \leqslant 0.45$ range (Zurman-Nasution *et al.* 2020). A single large LEV affects the flow even at height $0.1C$, as previously pointed out by double-headed cyan arrows in figures 3(*b*) and 3(*c*).

This 2-D flow cannot be maintained at higher *Re*, as seen in figures 4(*b*,*c*). The flapping foil generates LEVs near the leading edge during the suction phase of each cycle, alternately on the upper or lower side. There is a single LEV at $Re = 10^4$, but the flow

https://doi.org/10.1017/jfm.2026.11951 Published online by Cambridge University Press

produces smaller, more compact vortices and in much greater quantities as Re increases. These vortices are advected downstream and become unstable as the boundary layer grows, evolving into fully 3-D vortex structures from approximately $0.4C$ to the last half of the chord length. As expected, the flow at $Re = 10^6$ is noisier and more chaotic than at lower Re, especially near the trailing edge.

The normalised LEV volume or V^*_{LEV} in figure 4(e) represents the reduction of the LEV centroid region ($\lambda_2 < 0$) with increasing Re, which is further referred to as LEV size reduction. The LEV size increases slightly during its appearance in the second half of the cycle ($0.5 \leqslant t/T \leqslant 1$), but the ordering with respect to Re remains unchanged. Each LEV circulation increases with Re (data not presented for conciseness), but the normalised volume decreases substantially, indicating increased LEV compactness with an increased quantity of smaller LEVs. The LEV vorticity-weighted streamwise velocity u^*_{LEV} in figure 4(d) is seen to increase during the last half of the cycle following the increase in Re, indicating an increase in advection speed.

3.4. *The phase evolution of velocity profiles and near-wall pressure gradients*

We found that the extended laminar profile at each location on the foil or the relaminarisation described in § 3.1 is promoted by the FPG, whereas APG reverses it. The green arrows on the freestream pressure gradient in figure 3(c) can be compared to the pressure gradient near the wall in figure 5(b). The freestream region outside the boundary layer acts as forcing, accelerating the flow inside the boundary layer, as shown in figure 5(a) (circled 2). This FPG acceleration causes the velocity profile to rapidly inflate the laminar-like region of the boundary layer. The whole boundary layer might not inflate, as the FPG tends to reduce the boundary-layer momentum or displacement thicknesses. This expanding laminar part of the boundary layer is also more prominent with the increase of Re, with the $Re = 10^6$ boundary layer tripling in size for $t/T = 0.43{-}0.53$. Hence the relaminarisation is stronger at higher Re.

On the contrary, the APG reverses the expansion of the laminar region. When the flow is at the APG, the relaminarisation process is reversed as in figure 5 marked by circled 1 and also circled 3. The extended laminar regions shrink during this phase as they move away from the linear curve $u^+ = y^+$ and closer to the log profile. However, the shrinkage order based on increasing Re at circled 3 no longer follows the same trend as in circled 1. This is because the advection at circled 3 of vortex breakdown now influences the flow in addition to the APG condition.

Heat maps in figure 5(b) show that pressure gradients at the wall differ for each Re. The breakdown of vortices is related to the pressure gradient distribution, as indicated by the flickering blue–red areas just after phase $t/T = 0.5$. The LEVs at higher Re are smaller but more compact, experiencing faster advection, and thus have a shorter spatial footprint and reduced interaction with the wall. We see the same 'branching' APG for $Re = 10^4$ as explained in § 3.2 at figure 3(c) for pressure gradient. One ends before $t/T = 1$, while the other transports an LEV to the next cycle. The phase interval $\Delta t/T$ spent by smaller vortices for higher Re advected downstream is a half-cycle or less, while an LEV at $Re = 10^4$ needs a 1.5 times longer interval. The arrow marked by circled 3 is at the onset of LEV advection for $Re = 10^4$, while it is inside the advection region of LEV breakdown for $Re = 10^5$, and has just passed through at $Re = 10^6$. The reverse effect of relaminarisation ends faster at higher Re due to faster advection.

https://doi.org/10.1017/jfm.2026.11951 Published online by Cambridge University Press

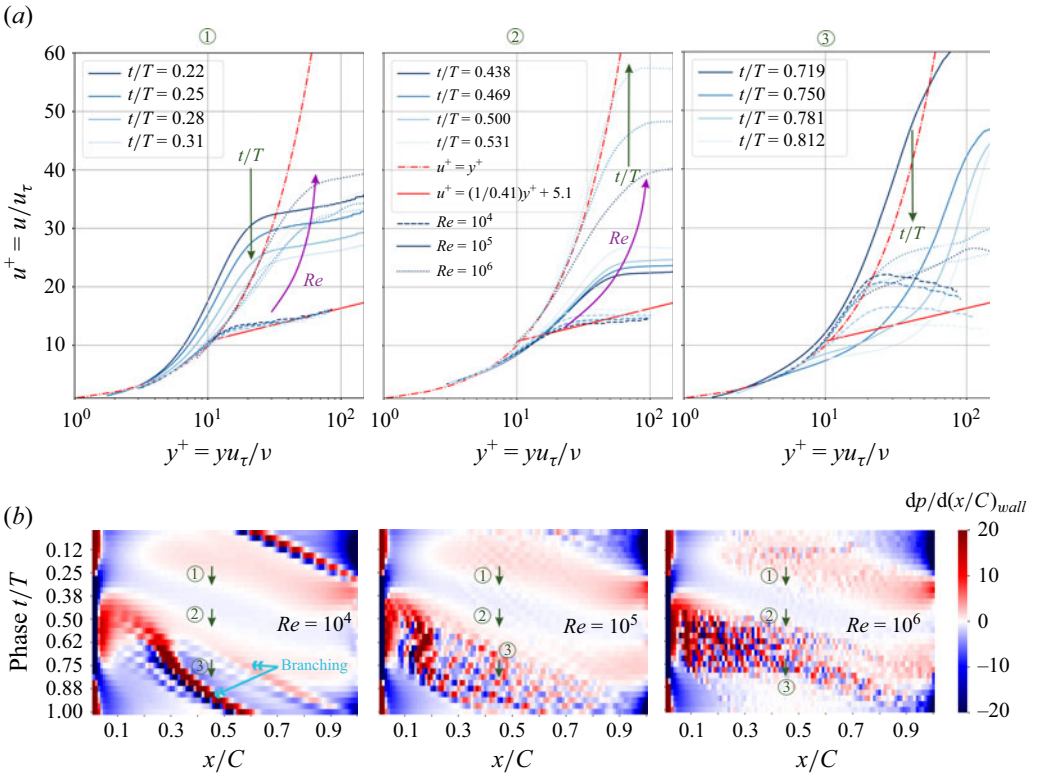


Figure 5. (*a*) Evolution of velocity profiles when exiting APG (circled 1), exiting FPG (circled 2), and inside vortex breakdown region (circled 3) at $x/C = 0.45$. (*b*) Heat maps of the near-wall pressure gradient for increasing *Re*. Green arrows follow the direction of increasing phase t/T, and the magenta arrow shows the trend of increasing *Re*. Velocity profiles and wall pressure gradients $\mathrm{d}p/\mathrm{d}(x/C)_{wall}$ are span- and phase-averaged.

3.5. *Indication of relaminarisation and cyclic behaviour*

Figure 6(*a*) illustrates the cyclic evolution of the normalised boundary layer edge velocity u_e/U_∞, the zero-mean fluctuation of wall-friction coefficient c_f', friction velocity u_τ, displacement thickness δ^*, and shape factor H at approximately mid position, $x = 0.45C$. Here, c_f' is the zero-mean fluctuation of $c_f = 2(u_\tau/u_e)^2$, where the average across phase t/T is removed at each position x/C. During the expansion of the laminar-like region marked by circled 2 (the same as in figures 3(*b*) and 5), the freestream velocity is positive and the flow is accelerating or at FPG state. Region circled 2 begins with the peak of c_f', followed by a rapid decrease by 31 % for an eighth of a cycle. Mukund *et al.* (2006) and Uzun & Malik (2021) found a similar trend of decrease. This condition is accompanied by an 8.5 % increase in H. On the contrary, the APG areas of circled 1 and circled 3 indicate an increase of c_f' by double and 62 %, along with the decrease of H by 15 % and 2 %. Friction velocity u_τ follows the same trend as c_f', with a slight delay. Displacement δ^* is at its lowest value during FPG, with a sudden increase by 35 % occurring at circled 3 mostly due to the APG region and downstream vortices. However, no clear trend can be inferred during the APG at circled 1 and the FPG at circled 2 due to subtle variations. Both boundary-layer displacement δ^* and momentum thickness θ (not shown) show a similar trend.

https://doi.org/10.1017/jfm.2026.11951 Published online by Cambridge University Press

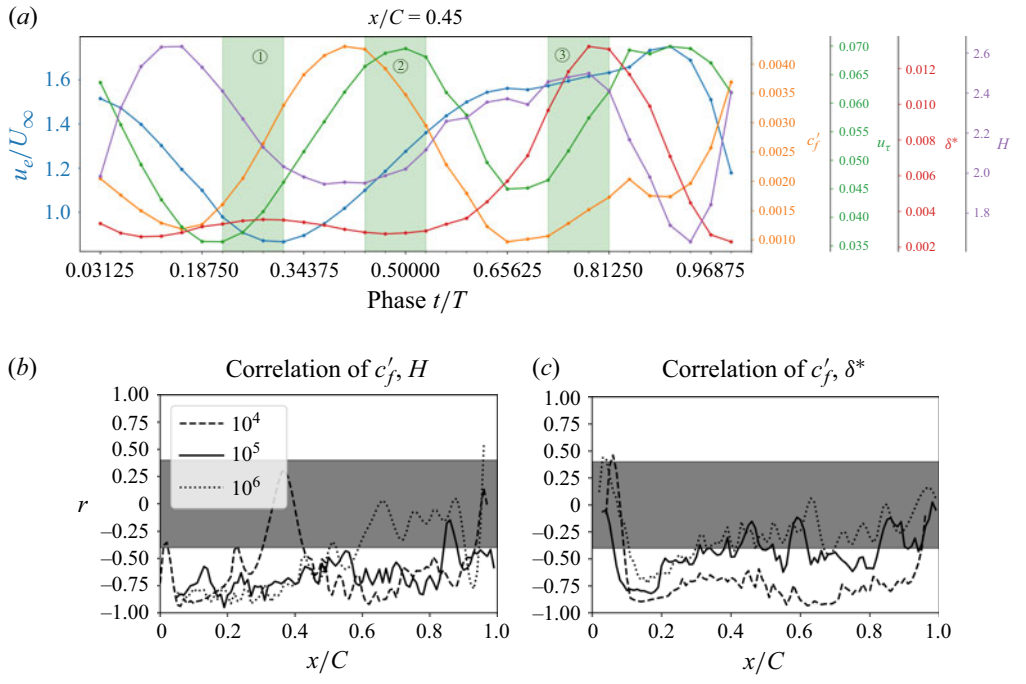


Figure 6. (*a*) Evolution of variables per cycle at $Re = 10^5$ and position $x/C = 0.45$. Values are span- and phase-averaged. Green-shaded areas correspond to green arrows in figure 5. The correlation of c_f' with (*b*) H and (*c*) δ^* is quantified using Pearson's correlation coefficient r. The moderate-to-high positive or negative correlations are defined by $|r| \geqslant 0.45$, whereas the grey-shaded region denotes weak correlation.

The consistent trend of H following the inverse variation of c_f' throughout the flapping cycle indicates that both quantities respond to the same near-wall momentum redistribution. The cyclic evolutions of H are closely related to c_f', as shown in figure 6(*b*) by moderate to strong inverse correlation on each position on the foil. At $Re = 10^6$ and $x/C > 0.6$, the correlation decreases due to the high signal-to-noise ratio in phase-averaging, but it does not diminish the overall trend. In contrast, the correlation between c_f' and displacement thickness δ^* (similarly for θ) in figure 6(*c*) is inconsistent and generally weaker at both the highest and the lowest Re across nearly all positions on the foil. This difference suggests that H is strongly associated with the inner-layer dynamics, or sensitive to profile reshaping, whereas thickness measures are more influenced by global boundary-layer growth. Even though classical equilibrium laminar–turbulent interpretations might not fully apply to flapping foil flow, H remains a physically interpretable measure.

Graphs in figure 7 demonstrate that each location x/C exhibits a cyclic behaviour of the friction coefficient fluctuation c_f' that intermittently approaches either laminar or turbulent limits. Here, the laminar correlation is presented by the Blasius line, where $c_f = (0.664^2)/Re_\theta$, and turbulent at ZPG by the Coles–Fernholz correlation, where $c_f = 2((1/0.41)\log(Re_\theta) + 4.127)^{-2}$. Increasing global Re also increases Re_θ, shifting the cycles to the right-hand side of the graph. However, each chordwise location exhibits different cyclic behaviours. Near the upstream locations ($x/C = 0.2$), the c_f' cycles are closely aligned with the Blasius or laminar correlation limit even for $Re = 10^6$. Moving closer to the trailing edge at $x/C = 0.72$, they begin to approach the turbulent correlation

https://doi.org/10.1017/jfm.2026.11951 Published online by Cambridge University Press

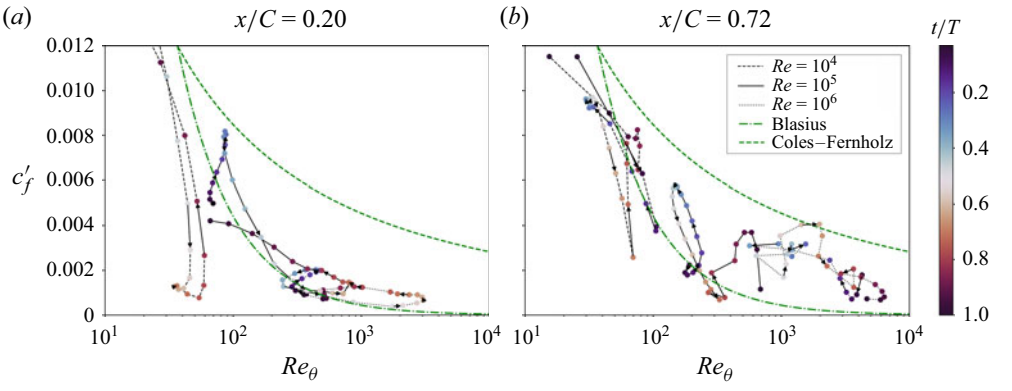


Figure 7. Cyclic behaviour of c_f' at $x/C = 0.2$ and 0.72 for different *Re*. Correlation lines are shown for Blasius (laminar) and Coles–Fernholz (turbulent). Arrows and colours (see legend) show forward in phase t/T. Low-*Re* cycles are closer to laminar, but the higher-*Re* cycles intermittently switch between laminar and turbulent.

line, especially at higher *Re*. Figure 7 indicates that most cycles at $Re = 10^4$ stay laminar, while c_f' at higher *Re* indicates a cyclic behaviour between laminar and turbulent.

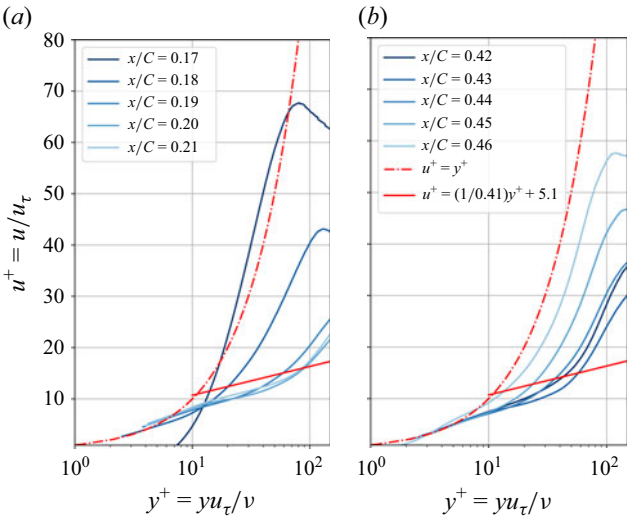
3.6. *Failure of the standard relaminarisation criteria*

Several criteria for relaminarisation or flow reversion are summarised by Narasimha & Sreenivasan (1979) from various studies based on the velocity profile deviations from the standard log law in steady or quasi-steady cases. These criteria are systematically proven to be inconsistent when applied as a diagnostic benchmark for flapping foil flows. Criteria for relaminarisation occur when $K = (\nu/\rho u_e^2)(\mathrm{d}u_e/\mathrm{d}x) \gtrsim 3.5 \times 10^{-6}$, $\Delta_p = -(\nu/\rho u_\tau^3)\ (\mathrm{d}p/\mathrm{d}x)|_{wall} \gtrsim 0.025$ and $\Delta_\tau = (\nu/u_\tau^3)(\mathrm{d}\tau/\mathrm{d}y)\big|_{wall} \lesssim 0.009$.

Figure 8 illustrates the velocity profile evolution on sequential chordwise positions in one phase, and the alignment with the standard log law. Figure 8(*a*) shows a decelerating flow where we observe a deviation of velocity profiles from the log law at positions $0.17 \leqslant x/C \leqslant 0.18$, while $0.19 \leqslant x/C \leqslant 0.21$ reverts to the log law. However, K falls below its criterion starting at $x/C \geqslant 0.18$, earlier than the change observed in velocity profiles. The Δ_τ values fall below zero, while Δ_p increases, indicating APG, but neither aligns with the criteria. Figure 8(*b*) shows an accelerating flow, where relaminarisation and deviations from the log law are expected at $x/C \geqslant 0.42$. Also, K exceeds its criterion later at $x/C \geqslant 0.43$, Δ_p exceeds the criterion only within $0.44 \leqslant x/C \leqslant 0.45$, and Δ_τ remains below the criterion throughout.

The inconsistencies with flow-reversion limits mentioned in the literature might be attributed to the reliance on a constant pressure gradient and the absence of phase-history effects. While their applicability to strongly unsteady boundary layers in flapping foils is expected to be limited, their predictive capability is systematically assessed as a baseline for comparison. Subtracting the influence from upstream flow or previous phases requires a more controlled condition. Any apparent agreement with the log law should be interpreted as a transient behaviour rather than a sustained equilibrium state. The obvious indications of the log-law departure for the flapping foil observed in this study occur when the friction coefficient c_f' decreases while the shape factor increases above the transitional turbulence $H \gtrsim 1.8$. Determining precise limits remains a topic for future work.

https://doi.org/10.1017/jfm.2026.11951 Published online by Cambridge University Press



x/C	H	Re_θ	Δ_p	Δ_τ	K	c_f'
0.17	3.46	486	−7.68	1.0×10^{-5}	4.5×10^{-6}	4.9×10^{-4}
0.18	2.35	668	−1.29	-1.0×10^{-3}	-1×10^{-5}	1.2×10^{-3}
0.19	1.90	713	−0.19	-6.6×10^{-4}	-1.3×10^{-5}	2.9×10^{-3}
0.20	1.78	707	0.047	-5.2×10^{-4}	-5.8×10^{-6}	3.6×10^{-3}
0.21	1.78	716	0.050	-4.9×10^{-4}	-1.3×10^{-6}	3.4×10^{-3}
0.42	2.28	733	−0.67	-6.5×10^{-4}	-1.5×10^{-5}	1.8×10^{-3}
0.43	2.20	725	−0.10	-8.1×10^{-4}	4.5×10^{-6}	2.3×10^{-3}
0.44	2.31	729	0.383	-7.5×10^{-4}	1.2×10^{-5}	1.7×10^{-3}
0.45	2.51	742	0.704	-3.7×10^{-4}	1.2×10^{-5}	1.1×10^{-3}
0.46	2.60	758	−0.80	6.7×10^{-4}	5.1×10^{-6}	7.0×10^{-4}

Figure 8. (*a*) Decelerating and (*b*) accelerating flow (relaminarisation) at phase $t/T = 0.75$ at $Re = 10^5$ are observed for the deviation from the standard log law. The variable nominals are indicated in the table.

3.7. *Wall friction fluctuation and the Clauser parameter*

The previous subsections provide a clear indication that both the shrinkage and contraction of the laminar-like regions are directly related to the wall friction coefficient fluctuation (c_f'). Therefore, it is essential to examine how it behaves with increasing Re.

Figures 9(*a*,*b*) are heat maps of the friction coefficient c_f and the friction velocity u_τ variables for $Re = 10^5$, where the trace of vortex breakdown is seen in the phase region $0.5 \lesssim t/T \lesssim 1$. Similar patterns of vortex advection are observed at other Reynolds numbers (refer to Appendix A), although each Re exhibits distinct fluctuation distributions. The lowest values, depicted in the lightest colour, are primarily observed in the region of LEV breakdown and its advection towards the trailing edge. Lower c_f values are associated with turbulence.

We obtain the cyclic fluctuation across a cycle T for c_f and u_τ by zeroing the mean values at each x/C from heat maps in figures 9(*a*,*b*). To compare fluctuations across different Re, we compute the standard deviation of c_f and u_τ, or zero-mean root mean square (RMS) in figures 9(*c*,*d*). The c_f RMS decreases with the increase of Re, likely due

https://doi.org/10.1017/jfm.2026.11951 Published online by Cambridge University Press

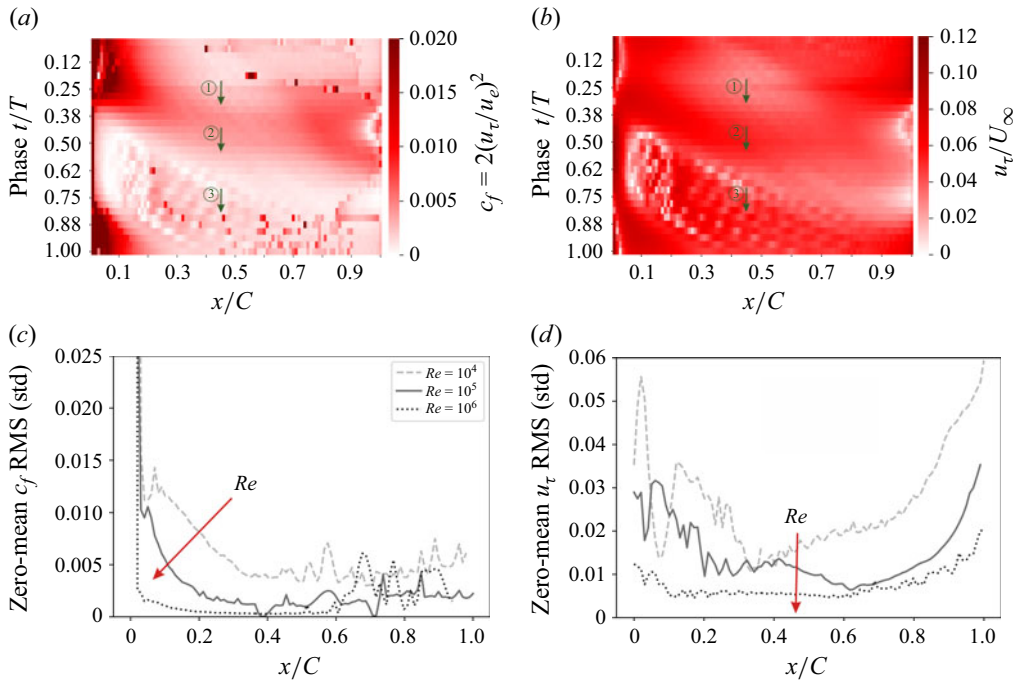


Figure 9. Heat maps of (*a*) the wall friction coefficient c_f and (*b*) friction velocities u_τ of $Re = 10^5$ along the streamwise location and phase. The zero-mean RMS (or standard deviation) of (*c*) c_f and (*d*) u_τ with increasing Re represents the fluctuation along the phases. Here, c_f and u_τ are span- and phase-averaged.

to the decrease of the u_τ RMS, even though the velocities at the freestream or boundary-layer edge are similar for all Re. Increased Re generates multiple, smaller, more compact vortices, causing early and rapid vortex breakdown. This reduces the coherence and phase-localised vortex–wall interaction, leading to a smaller peak-to-trough cyclic modulation of wall shear, i.e. lower c_f RMS and u_τ RMS. In Appendix A, $Re = 10^4$ exhibits the highest contrast between the LEV area and its surroundings at the leading edge, explaining this high fluctuation across the cycle phase or higher RMS. The flow remains turbulent near the trailing edge at $Re = 10^6$, mainly because the fluctuation of u_τ increases, or the turbulence level is stronger. The moderation of c_f RMS towards the trailing edge, unlike u_τ, is caused by the increase of the denominator u_e values and u_e RMS.

Figure 10 illustrates the normalised pressure gradient parameter of Clauser (1954) as $\beta_{RC} = (\delta^*/\tau_w)(\mathrm{d}p/\mathrm{d}x)$. Identical values of β_{RC} indicate the same ratio of pressure gradient over wall shear stress, and a similar shape factor under certain conditions. Positive values indicate APG, and negative values indicate FPG. The β_{RC} are distributed similarly to the near-wall pressure gradient in figure 5(*b*), with two significant APG regions. However, we can more clearly observe the regions where LEVs are first generated (marked 'LEV'), followed by their downstream advection traces in later phases. With increasing Re, the LEV influence is pushed closer to the leading edge, a sign of early LEV generation. At $Re = 10^6$, the LEV region narrows significantly and is much closer to the foil's leading edge at $t/T \approx 0.5$. The LEV breakdown is also advected downstream, along with the second APG region in the opposite β_{RC} sign, as if it were disconnected from the region where the LEV was initially generated. It might explain why regions of downstream advection at $Re = 10^6$ are not affected by the large LEV region nor promoted into fully 3-D

https://doi.org/10.1017/jfm.2026.11951 Published online by Cambridge University Press

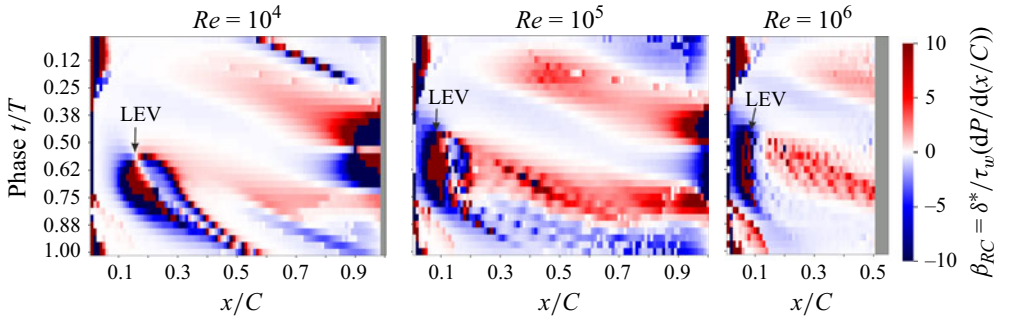


Figure 10. Clauser's pressure gradients parameter β_{CL} normalised by displacement thickness δ^* and wall shear stress τ_w (Clauser 1954). Greys have no data, and only the first front halves of the chord locations are provided for $Re = 10^6$ due to a high signal-to-noise ratio.

turbulence. It also explains why c_f and u_τ RMS in figure 9 are smaller with increasing Re. The early and narrow LEV-generated region is somehow beneficial for stabilising the LEV breakdown at higher Re.

In conclusion, the FPG that promotes the expansion of the laminar-like region is not affected by the flow fluctuations caused by the breakdown of LEVs. As a result, higher Re may lead to more stable or undisturbed relaminarisation. It would be interesting to investigate in the future whether this phenomenon continues to occur at even higher Re.

4. Conclusion

We study the flow across three increasing Reynolds numbers, $Re = 10^4$, 10^5 and 10^6, at the optimum propulsive range of flapping foil $St = 0.3$. We show that despite the similarity of freestream being given as forcing variables, different Reynolds number cases show unique trends for the variables inside the boundary layer. The freestream pressure (Cp) and velocity (u_{10C}/U_∞) variables show similarities to the prescribed kinematics that are dominant in the region far from the boundary layer. We notice that the Cp trend is almost constant throughout the foil position x/C, but changes with phases following the heave kinematics. Meanwhile, u_{10C}/U_∞ resembles the trend of pitch kinematics where each x/C varies in the vertical position Y from the leading edge to the trailing edge per phase. Both velocity and pressure gradient at the freestream exhibit the half-cycle advection trend as the prescribed sinusoidal kinematics.

The near-wall dynamics is governed by the LEV formation and breakdown. During the first half-cycle, before vortex breakdown, the wall pressure gradient follows the freestream pressure gradient. It indicates the strong influence of flapping kinematics on the flow. Under strong FPGs, the flow exhibits relaminarisation with a growing laminar-like region, consistent with Warnack & Fernholz (1998). The second half of the flapping foil cycle is strongly influenced by LEV breakdown, which modifies the downstream boundary-layer development in subsequent phases. As the Reynolds number increases, the flapping foil generates more LEVs of a much smaller size and greater compactness, with reduced normalised volume but increased strength. They advect more rapidly, as indicated by increasing vorticity-weighted streamwise velocity, resulting in shorter vortex–wall interaction times.

Although higher Re generally promotes turbulence and separation, the phase-to-phase fluctuation of the friction coefficient (c_f RMS) decreases with increasing Re. This reflects reduced cyclic wall-shear modulation. The trend is associated with the observed

https://doi.org/10.1017/jfm.2026.11951 Published online by Cambridge University Press

confinement of the LEV-generation region towards the leading edge, which extends the downstream breakdown region and promotes earlier vortex breakdown. The increase in LEV compactness, faster advection, the confinement of the formation region, and the reduced wall-shear cyclic fluctuations lead to more persistent laminar-like behaviour at $Re = 10^6$.

Classical relaminarisation indicators under FPG proposed by Narasimha & Sreenivasan (1979) do not consistently capture the present flapping foil flows. Instead, a decrease in the cyclic fluctuation of the friction coefficient c_f' and an increase in the shape factor H during the acceleration of outer flow ($\mathrm{d}u_e/\mathrm{d}(x/C) > 0$) provide more consistent diagnostic trends. However, defining a single global scaling for relaminarisation across phases remains challenging due to upstream conditions, phase history and LEV breakdown. Similar scaling difficulties in non-equilibrium boundary layers have been discussed by Marusic *et al.* (2010), and are inherent to flapping foil flows.

The reduced phase-to-phase fluctuations of c_f at increasing Re indicate a reduction of near-wall unsteadiness, as laminar-like behaviours persist. Resolving the flow at $Re > 10^6$ would require substantially higher computational resources to determine whether turbulence eventually dominates over kinematic forcing. Fukagata *et al.* (2023) show drag reduction of up to 40 % due to persistent streamwise relaminarisation even at $Re_\tau = 10^5$ in the downstream travelling wave experiment. This implies that kinematics may remain dominant in propulsive flapping foil flows, even beyond $Re = 10^6$. Such behaviour may be of interest for drag and noise reduction studies. Moreover, the persistent laminar-like behaviours facilitate numerical simulations at high Re, reducing near-wall resolutions compared to stationary foil simulations at stall. Extending the present analysis to non-propulsive flapping states (e.g. $St > 0.5$), where stronger instabilities and more chaotic wakes are expected, remains an important direction for future work but lies beyond the scope of the present study.

Acknowledgements. The authors would like to thank the Defence Science and Technology Laboratory UK for the earlier funding, and the IRIDIS High-Performance Computing Facility with its associated support services at the University of Southampton. They would also like to thank Professor U. Piomelli and Dr T. Nishino for informal email discussions and valuable feedback.

Declaration of interests. The authors report no conflict of interest.

Data availability statement. Data published in this article are available from the University of Southampton repository at https://doi.org/10.5258/SOTON/D3974.

Appendix A

Nominal values of wall friction coefficient c_f and the friction velocity u_τ for different Re are shown in figure 11.

https://doi.org/10.1017/jfm.2026.11951 Published online by Cambridge University Press

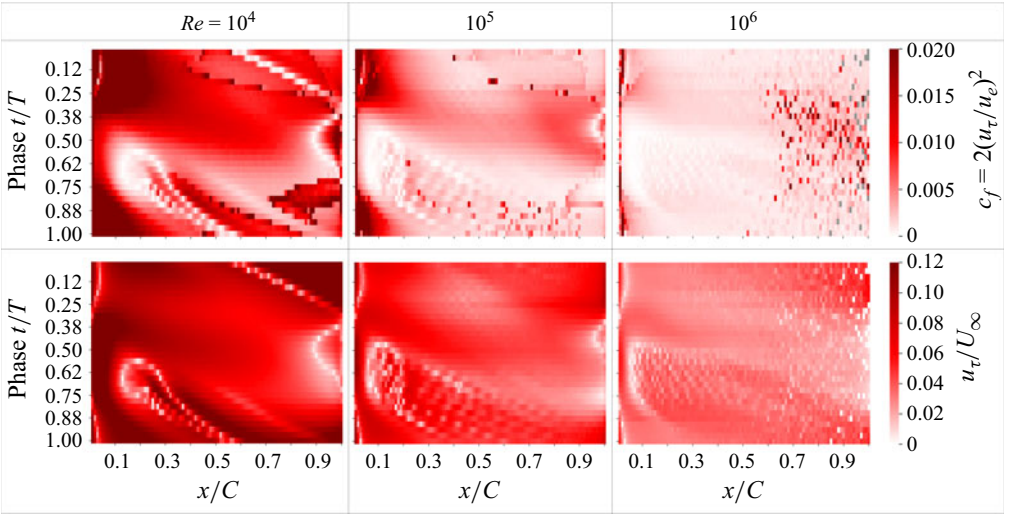
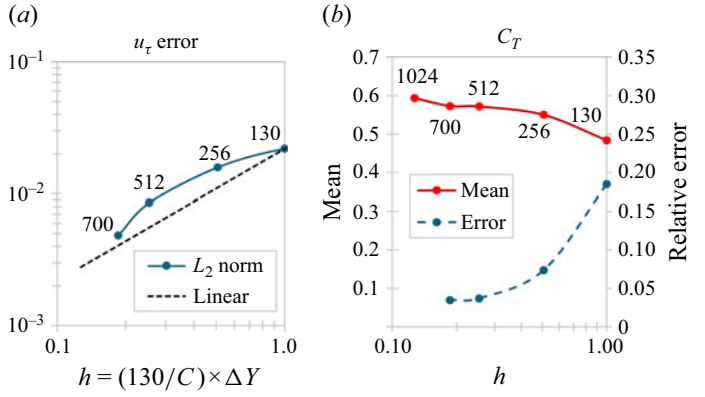


Figure 11. Nominal values of friction coefficient c_f and friction velocities u_τ of increasing Reynolds number presented on heat maps along the phases t/T and positions on foil x/C. Grey cells show no values. The nominal values are decreasing with Re, creating a more uniform map across the phase and location, thus decreasing the fluctuation generally.



$C/\Delta Y$	$\overline{y^+}$	y^+ range
130	4.0	[0.2, 7.0]
256	2.5	[0.14, 4.6]
512	1.5	[0.07, 3.1]
700	1.2	[0.02, 2.7]
1024	0.9	[0.03, 2.2]

Figure 12. The grid convergence study at $Re = 10^4$ is presented by: (a) the L_2 norm $\sqrt{(1/N)\sum_{i=1}^{N}(\sigma^{h_{finest}}(i) - \sigma^{h}(i))^2}$, where $\sigma(i)$ represents the zero-mean RMS of u_τ at the $i = x/C$ location, for $N = 100$ equispaced points along the chord C, and resolution h; (b) the mean thrust coefficient C_T and relative errors $(C_T - C_{T_{finest}})/C_{T_{finest}}$. The u_τ RMS at $C/\Delta Y = 700$ corresponds to the same values presented in figure 9(d). The table summarises the grid resolutions $C/\Delta Y$ with the mean and a range of y^+ values.

Appendix B

The results in figure 12(a) present a grid-convergence study of the zero-mean RMS of u_τ, a near-wall cyclic-fluctuating quantity, exhibiting a first-order trend and decreasing monotonically with the grid refinement. The same grid-scaling strategy approximately translates to higher Reynolds number cases, with increasing y^+ in proportion to u_τ. The mean and range of the near-wall resolution y^+ remain within $y^+ \leqslant 7$, and the C_T relative errors are within 18 % in figure 12(b) for the coarsest grid. Presenting

https://doi.org/10.1017/jfm.2026.11951 Published online by Cambridge University Press

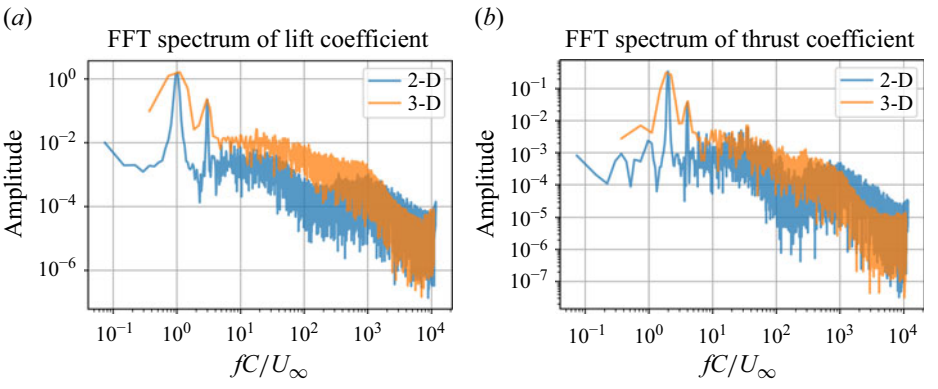


Figure 13. The fast Fourier transform (FFT) spectra of (*a*) lift (C_L) and (*b*) thrust (C_T) coefficients from 2-D and 3-D simulations at $Re = 10^5$ and $St = 0.3$, representing pressure and viscous forces.

relative errors is conservative due to the near-zero values of C_T, even though the absolute differences are small. A full convergence study at higher Reynolds numbers is computationally prohibitive, yet the trend consistency supports the robustness of the numerical set-up.

Appendix C

Figure 13 shows that both 2-D and 3-D simulations exhibit a dominant peak and the second harmonic of flapping frequency, confirming that the primary flapping-driven unsteady mechanism is preserved in both cases. The 3-D simulation displays noticeably higher broadband energy across intermediate and high frequencies compared to the 2-D simulation. This indicates the presence of additional 3-D flow structures and spanwise instabilities that redistribute energy towards smaller scales. The same conclusion is valid for $Re = 10^4$ and $Re = 10^6$.

The fast Fourier transform shows that the fundamental harmonic is unchanged between the 2-D and 3-D cases, indicating that the global lift and thrust remain kinematically governed, while the enhanced broadband content in the 3-D case reflects additional vortex deformation and breakdown. Thus 3-D effects introduce small-scale unsteadiness without altering the primary flapping-frequency response, consistent with spanwise LEV instability at this Reynolds number.

References

Ambrogi, F., Piomelli, U. & Rival, D.E. 2022 Characterization of unsteady separation in a turbulent boundary layer: mean and phase-averaged flow. *J. Fluid Mech.* **945**, A10.

Anderson, E.J., McGillis, W.R. & Grosenbaugh, M.A. 2001 The boundary layer of swimming fish. *J. Expl Biol.* **204** (1), 81–102.

Balin, R. & Jansen, K.E. 2021 Direct numerical simulation of a turbulent boundary layer over a bump with strong pressure gradients. *J. Fluid Mech.* **918**, A14.

Benton, S.I. & Visbal, M.R. 2018 The onset of dynamic stall at a high, transitional Reynolds number. *J. Fluid Mech.* **861**, 860–885.

Clauser, F.H. 1954 Turbulent boundary layers in adverse pressure gradients. *J. Aeronaut. Sci.* **21** (2), 91–108.

Coles, D. 1956 The law of the wake in the turbulent boundary layer. *J. Fluid Mech.* **1** (2), 191–226.

Devenport, W.J. & Lowe, K.T. 2022 Equilibrium and non-equilibrium turbulent boundary layers. *Prog. Aerosp. Sci.* **131**, 100807.

Eloy, C. 2012 Optimal Strouhal number for swimming animals. *J. Fluids Struct.* **30**, 205–218.

https://doi.org/10.1017/jfm.2026.11951 Published online by Cambridge University Press

FUKAGATA, K., IWAMOTO, K. & HASEGAWA, Y. 2023 Turbulent drag reduction by streamwise traveling waves of wall-normal forcing. *Annu. Rev. Fluid Mech.* **56** (1), 69–90.

GRIFFIN, K.P., FU, L. & MOIN, P. 2021 General method for determining the boundary layer thickness in nonequilibrium flows. *Phys. Rev. Fluids* **6** (2), 024608.

HOVER, F.S., HAUGSDAL, O. & TRIANTAFYLLOU, M.S. 2004 Effect of angle of attack profiles in flapping foil propulsion. *J. Fluids Struct.* **19** (1), 37–47.

JIMÉNEZ, J. & MOIN, P. 2006 The minimal flow unit in near-wall turbulence. *J. Fluid Mech.* **225**, 213–240.

MAERTENS, A.P. & WEYMOUTH, G.D. 2015 Accurate Cartesian-grid simulations of near-body flows at intermediate Reynolds numbers. *Comput. Meth. Appl. Mech. Engng* **283**, 106–129.

MARUSIC, I., MCKEON, B.J., MONKEWITZ, P.A., NAGIB, H.M., SMITS, A.J. & SREENIVASAN, K.R. 2010 Wall-bounded turbulent flows at high Reynolds numbers: recent advances and key issues. *Phys. Fluids* **22** (6), 065103.

MUKUND, R., VISWANATH, P.R., NARASIMHA, R., PRABHU, A. & CROUCH, J.D. 2006 Relaminarization in highly favourable pressure gradients on a convex surface. *J. Fluid Mech.* **566**, 97–115.

MÜNCH, C., AUSONI, P., BRAUN, O., FARHAT, M. & AVELLAN, F. 2010 Fluid–structure coupling for an oscillating hydrofoil. *J. Fluids Struct.* **26** (6), 1018–1033.

NA, Y. & MOIN, P. 1998 Direct numerical simulation of a separated turbulent boundary layer. *J. Fluid Mech.* **374**, 379–405.

NARASIMHA, R. & SREENIVASAN, K.R. 1979 Relaminarization of fluid flows. *Adv. Appl. Mech.* **19**, 221–309.

PATEL, V.C. & HEAD, M.R. 1968 Reversion of turbulent to laminar flow. *J. Fluid Mech.* **34** (2), 371–392.

SCHLICHTING, H. & KESTIN, J. 1979 *Boundary-Layer Theory*, 7th edn. McGraw-Hill.

TANEDA, S. & TOMONARI, Y. 1974 An experiment on the flow around a waving plate. *J. Phys. Soc. Japan* **36** (6), 1683–1689.

TRIANTAFYLLOU, G.S., TRIANTAFYLLOU, M.S. & GROSENBAUGH, M.A. 1993 Optimal thrust development in oscillating foils with application to fish propulsion. *J. Fluids Struct.* **7** (2), 205–224.

TRIANTAFYLLOU, M.S., TECHET, A.H., ZHU, Q., BEAL, D.N., HOVER, F.S. & YUE, D.K. 2002 Vorticity control in fish-like propulsion and maneuvering. *Integr. Compar. Biol.* **42** (5), 1026–1031.

UZUN, A. & MALIK, M.R. 2021 Simulation of a turbulent flow subjected to favorable and adverse pressure gradients. *Theor. Comput. Fluid Dyn.* **35** (3), 293–329.

VINUESA, R., NEGI, P.S., ATZORI, M., HANIFI, A., HENNINGSON, D.S. & SCHLATTER, P. 2018 Turbulent boundary layers around wing sections up to $Re_c = 1\,000\,000$. *Intl J. Heat Fluid Flow* **72**, 86–99.

WARNACK, D. & FERNHOLZ, H.H. 1998 The effects of a favourable pressure gradient and of the Reynolds number on an incompressible axisymmetric turbulent boundary layer. Part 2. The boundary layer with relaminarization. *J. Fluid Mech.* **359**, 357–381.

WEYMOUTH, G.D. & YUE, D.K.P. 2011 Boundary data immersion method for Cartesian-grid simulations of fluid–body interaction problems. *J. Comput. Phys.* **230** (16), 6233–6247.

YANASE, K. & SAARENRINNE, P. 2015 Unsteady turbulent boundary layers in swimming rainbow trout. *J. Expl Biol.* **218** (9), 1373–1385.

ZURMAN-NASUTION, A.N., GANAPATHISUBRAMANI, B. & WEYMOUTH, G.D. 2020 Influence of three-dimensionality on propulsive flapping. *J. Fluid Mech.* **886**, 1–14.

ZURMAN-NASUTION, A.N., WEYMOUTH, G.B. & GANAPATHISUBRAMANI, B. 2024 Near-wall flow characteristics of flapping foils at $Re = 1\,000\,000$. In *Proceedings of the Cambridge Unsteady Flow Symposium 2024* (ed. J.C. Tyacke & N.R. Vadlamani), pp. 219–230. Springer Nature.

https://doi.org/10.1017/jfm.2026.11951 Published online by Cambridge University Press